Research Article

The Effect of the Nanoscale Structure of Nanobioceramics on Their *In Vitro* Bioactivity and Cell Differentiation Properties

Cristian Covarrubias,[1] Fabiola Arroyo,[1] Consuelo Balanda,[1] Miguel Neira,[1] Alfredo Von Marttens,[2] Pablo Caviedes,[3] Juan Pablo Rodríguez,[4] and Carla Urra[4]

[1]*Laboratory of Nanobiomaterials, Institute for Research in Dental Sciences, Faculty of Dentistry, University of Chile, 8380492 Santiago, Chile*

[2]*Department of Prosthesis, Faculty of Dentistry, University of Chile, 8380492 Santiago, Chile*

[3]*ICBM, Faculty of Medicine, University of Chile, 8380492 Santiago, Chile*

[4]*Laboratory of Cell Biology, INTA, University of Chile, 8380492 Santiago, Chile*

Correspondence should be addressed to Cristian Covarrubias; ccovarru@u.uchile.cl

The effect of the nanoscale structure of bioceramics on their *in vitro* bioactivity and capacity to osteogenically differentiate stem cell is studied. Nanoparticles of hydroxyapatite (nHA), bioactive glass (nBG), nanoporous bioactive glass (MBG), and nanoporous bioactive glass nanospheres (nMBG) are investigated. The nanometric particle size of bioceramics seems to be more determining in controlling the ability to induce bone-like apatite as compared to the nanoporous structure. At short incubation time, nBG also produces a bioactive extracellular medium capable of upregulating key osteogenic markers involved in the development of a mineralizing phenotype in DPSCs. The bioactive properties of nBG are promissory for accelerating the bone regeneration process in tissue engineering applications.

1. Introduction

Different techniques employing either autogenous or alloplastic materials have been used for decades as a filling material to repair bone dental defects, with variable degrees of success [1]. Bioceramics such as tricalcium phosphate (β-TCP), synthetic hydroxyapatite (HA), and bioactive glass (BG) appear as the most used alloplastic materials for bone repair. Most of the bioceramics stimulate the nucleation and crystallization of a biologically reactive hydroxycarbonate apatite (HCA) layer equivalent to the inorganic mineral phase of bone when contacted with physiological medium [2]. The growing HCA layer on the surface of the material provides an ideal environment for colonization by osteoblast bone-forming cells, followed by proliferation and differentiation of the cells to form new bone. In the case of BG, this biomaterial not only provides an osteoconductive and osteoproductive substrate, but also actively stimulates cells to express osteoblastic phenotypes [3]. It has been demonstrated that

the dissolution products of BG stimulate cell proliferation and the upregulation of a number of genes known to be involved in osteoblast metabolism and bone homeostasis. Most of the commercial biomaterial products are based on bioceramics particles with micrometer dimensions and prepared through high temperature processes. Nowadays, the advances in the synthesis of nanomaterials by sol-gel based techniques offer the possibility of synthesizing bioceramics with nanometric particle size, controlled nanostructures, and using relatively low processing temperatures. Nanodimensional bioceramics are expected to have improved bioactive properties due to their larger specific surface area. Smaller crystals and nanostructured surfaces dissolve more rapidly than microsized crystals of the same composition, due to the higher surface area exposed to the biological environment. Thus, nanosized bioceramics accelerate the rate of formation and growth of the biologically active apatite layer [4], improving the chemical link between the materials and the newly formed bone, as well as the later attachment and differentiation of

cells. Nanobioceramics with different particle size, nanostructure, crystallinity, and composition have been developed by using sol-gel based methods [5]. Nanohydroxyapatite (nHA) particles (30 nm) show similar morphology, size, and crystallinity to HA crystals of human hard tissues [6] and have demonstrated producing enhanced biomineralization and osteoblast functions [7–9]. Bioactive glass with nanometric particle size (nBG) induce substantially higher mineralization rate than the micrometric counterpart [10] and enable the production of composite tissue engineering with improved bioactivity and mechanical properties [11, 12]. The incorporation of supramolecular chemistry to the sol-gel processes has provided a new generation of bioactive glasses with highly ordered mesoporosity (MBG) [13]. Although MBG present particle size in the micrometer range, their internal structure is constituted of a highly ordered pore system with nanometric dimensions (4–7 nm). Its study has opened a new direction for applying nanotechniques to regenerative medicine by coupling material bioactivity with drug delivery of therapeutic molecules. MBG is highly bioactive compared with conventional ones, due to the increased surface area supplied by the nanoporosity. More recently, MBG nanoparticles (nMBG) with spherical morphology have been also prepared by a facile hydrothermal method [14]. This new bioactive glass structure combines a particle size of nanometric dimensions with the highly ordered porous nanostructure. Although the bioactivity of nMBG has not been compared with that of microsized MBG, they have demonstrated excellent bioactivity in SBF as well as a sustained release of antibone cancer drug. The literature indicates that in general bioceramics with nanoscale dimensions present superior bioactivity than their microsized counterpart. However, it is not clear what nanoscale property of the nanobioceramics is more decisive in controlling their bioactivity and how these properties affect their bioactive response. Nanoparticle size and shape, internal nanostructure, nanoporosity, surface area, crystallinity, or composition are properties that can differently affect the bioactive behavior of the nanobioceramics.

In the current work we synthesize and characterize different types of nanobioceramics (nHA, nBG, MBG, and nMBG) and systematically investigate the effect of their nanoscale structure on *in vitro* bioactivity in SBF, protein adsorption capacity, and osteogenic differentiation properties in presence of stem cells.

2. Materials and Methods

2.1. Synthesis of Nanobioceramics

2.1.1. Synthesis of Hydroxyapatite Nanoparticles. HA nanoparticles (nHA) were synthesized by the sol-gel precipitation method reported by Sanosh et al. [6]: 50 mL of 0.6 M potassium dihydrogen phosphate ($NH_4H_2PO_4$; May & Baker) solution was added dropwise to an equal volume of 1 M calcium nitrate ($Ca(NO_3)_2 \cdot 4H_2O$; Sigma-Aldrich) solution under constant stirring. Aqueous ammonia (NH_3) was added dropwise to the resulting solution until pH 11 was reached. The precipitated solution was stirred for 1 h and aged at room temperature for 24 h. The white precipitate was separated and

washed by repeated centrifugation and redispersion in fresh distilled water (three cycles). It was then dried at 40°C for 24 h, heated at a rate of 10°C/min to 200°C, and calcined at that temperature for 1 h. A calcination temperature of 200°C was chosen in order to obtain a less crystalline and more reactive nHA particle.

2.1.2. Synthesis of Bioactive Glass Nanoparticles. Nanosized BG particles (nBG) were synthesized by the sol-gel method initially reported by Hong et al. [15] and using a molar composition optimized by our group [11]: $58SiO_2 : 40CaO : 5P_2O_5$. The synthesis of nBG was carried out as follows: a calcium-based solution was prepared by dissolving 7.7 g of $Ca(NO_3)_2 \cdot 3H_2O$ (Sigma-Aldrich) in 117 mL of distilled water at room temperature. A second solution was prepared by diluting 9.7 mL of tetraethyl orthosilicate (TEOS 98%; Aldrich) in 63.5 mL of ethanol, and it was added to the calcium nitrate solution, and the pH of the resulting solution was adjusted to 1-2 with citric acid. This transparent solution was slowly dropped under vigorous stirring into a solution of 1.2 g of $NH_4H_2PO_4$ (May & Baker) in 1500 mL of distilled water. During the dripping process the pH was kept at around 10 with aqueous ammonia. The mixture was stirred for 48 h and aged for 48 h at room temperature. The precipitate was separated by centrifugation (12,000 rpm) and washed by three centrifugation-redispersion cycles with distilled water. The separated solid was dispersed in 200 mL of a 2% w/v aqueous solution of polyethylene glycol (PEG, 10,000) and stirred for 24 h. This suspension was freeze dried and then calcined at 700°C for 3 h to obtain a fine white nBG powder.

2.1.3. Synthesis of Mesoporous Bioactive Glass. Ordered mesoporous $58SiO_2$-$36CaO$-$6P_2O_6$ (mol.%) bioactive glass (MBG) was synthesized using the sol-gel/evaporation-induced self-assembly (EISA) technique [16]. The sol-gel synthesis solution was prepared by using TEOS, triethyl phosphate (TEP), $Ca(NO_3)_2 \cdot 3H_2O$ as SiO_2, P_2O_5, and CaO sources, respectively. This sol-gel solution was formed using HCl as catalyst in a water-ethanol media, and the nonionic surfactant Pluronic P123 as structure-directing agent. The resulting colorless sol was stirred at room temperature for 24 h and then was transferred into Petri dishes and evaporated at 40°C for ~7 days. The dried gel was removed as a homogeneous and transparent film and treated at 700°C for 3 h to obtain a white MBG powder.

2.1.4. Synthesis of Mesoporous Bioactive Glass Nanospheres. MBG nanospheres were synthesized by the hydrothermal method reported by Wu et al. [14] using cetyltrimethylammonium bromide (CTAB) and poly(vinylpyrrolidone) (PVP) as cotemplates. In a typical experiment, 1 g PVP and 0.46 g NaOH were firstly dissolved in 120 mL distilled water. Then, 1.4 g CTAB was added to the PVP–NaOH solution and stirred for 1 h. Then, tetrahydrate calcium nitrate ($Ca(NO_3)_2 \cdot 4H_2O$), tetraethyl orthosilicate (TEOS), and triethyl phosphate (TEP) were added with vigorous stirring. The molar ratio of Ca : P : Si is 15 : 5 : 80. After stirring for 24 h, the milk-like mixture was then sealed in Teflon-lined autoclaves at 80°C

for 48 h. The products were collected by centrifugation and washed by water and ethanol, 3 times with each. Then the collected powders were dried at 80°C overnight and calcined at 550°C for 5 h to remove any remaining PVP and CTAB.

2.2. In Vitro Bioactivity Assays.
The ability of the bioceramics to induce the formation of apatite was assessed in acellular SBF, which has inorganic ion concentrations similar to those of human extracellular fluid. The SBF solution was prepared as described by Kokubo et al. [17] using the standard ion composition (Na^+ 142.0, K^+ 5.0, Mg^{2+} 1.5, Ca^{2+} 2.5, Cl^- 147.8, HCO_3^- 4.2, HPO_4^{2-} 1.0, and SO_4^{2-} 0.5 mM). The fluid was buffered at physiological pH 7.4 at 37°C with tri-(hydroxymethyl) aminomethane and hydrochloric acid. For this purpose, circular pellets of 9 mm diameter and 2 mm thickness were prepared by compacting the bioceramic powder in an evacuable pellet die. The bioceramic pellets were individually soaked in 50 mL of SBF in polyethylene containers at 36.5°C using a thermostatic bath. After incubation for a designated time period, the bioceramics were removed from SBF, rinsed with distilled water, and dried at 60°C.

2.3. Material Characterization.
Bioaceramic nanomaterials and apatite formation in SBF were analyzed by X-ray diffraction (XRD). XRD patterns were measured on a Siemens D 5000 diffractometer using CuKα radiation within a 2θ range of 5–50° at a scanning speed of 1.2°/min. For XRD analysis, the bioceramic pellets were removed from SBF solution, then rinsed with distilled water, and dried at 60°C for 24 h. Bioceramics were also examined by Transmission Electron Microscopy (TEM) in a Philips Tecnai 12 Bio Twin microscope. Specimens were prepared by transferring a small drop of sample-ethanol suspension to carbon-film coated copper grids. The porous nanostructure of MBG and nMBG materials was examined by high resolution transmission electron microscopy (HRTEM) on a FEI-Tecnai G2 F20 S-Twin high-resolution transmission electron microscope equipped with a field emission gun operating at an accelerating voltage of 120 kV. Plan-view film specimens of MBG were prepared by removing the silica MBG films from the Petri dish and suspending them in ethanol. This suspension was then dispersed on a holey carbon film supported by a copper grid. The materials were also analyzed by scanning electron microscopy with a Jeol JSM 5410 microscope equipped with energy-dispersive X-ray spectroscopy (EDX) after coating the surfaces with gold. Chemical structure of the materials was characterized by attenuated total reflectance with Fourier transform infrared spectroscopy (ATR-FTIR) on an Agilent Cary 630 ATR-FTIR spectrometer. ATR-FTIR analysis of hydroxyl functional groups was performed after heat treatment of the samples at 150°C for 2 hours. Textural characterization of bioceramic nanomaterials was carried out by N_2 adsorption at 77 K in a Micromeritics ASAP 2010 sorptometer. The specific apparent surface areas (Sg) were obtained using the Brunauer-Emmett-Teller (BET) method. Pore diameter was estimated from the pore size distribution curves obtained by the Barrett-Joyner-Halenda model.

2.4. Protein Adsorption.
Bovine serum albumin (BSA) (Merck) was used as model protein. Solutions containing 0.4 mg/mL of protein were prepared in a pH 7.4 phosphate buffer (K_2HPO_4/KH_2PO_4 100 mM), and 1.5 mL of protein solution was contacted with the bioceramic pellet in a 20 mL glass vial and then incubated at 37°C for 6 h. The surfaces were then washed with phosphate buffer to remove the nonadherent proteins. Each sample was transferred to a 20 mL glass vial containing 1.5 mL of 2% sodium dodecyl sulfate solution and subsequently incubated at 37°C in a thermostatic bath for 12 h to extract adhered proteins. Protein concentration was determined using the spectrophotometric Micro Bicinchoninic Acid Assay Kit (Thermo Scientific) according to the manufacturer's instructions.

2.5. Ion Release Measurements.
The release of calcium, phosphate, and silicon ions from the bioceramics was measured up to 14 days of incubation in tris(hydroxymethyl)amino methane (Tris) buffer solution pH 7.4. 10 mL of Tris buffer solution was contacted with the bioceramic pellets (0.15–0.30 g) in a 20 mL glass vial and then incubated at 37°C. After completing the incubation period, the pellets were removed, and the resulting solution was centrifuged at 12,000 rpm for 20 min in order to eliminate loose bioceramic particles. The Ca^{2+} in the aqueous phase was analyzed with a HANNA HI4104 Calcium Polymer Membrane Combination Ion Selective Electrode. PO_4^{3-} concentration was determined by using the spectrophotometric method based on the ammonium molybdate reaction [18]. Soluble silicon species were analyzed by using an ASTM spectrophotometric method that determines molybdate-reactive soluble silicon species [19]. The concentration of ion released into the solution was expressed as ion concentration per bioceramic mass (mM/g).

2.6. Cell Culture.
Stem cells isolated from dental pulp (DPSCs) [20] were used to evaluate cell proliferation and differentiation in the presence of conditioned medium containing nanobioceramic dissolution products. 10 mg of nanobioceramic powder was added to 1 mL of Dulbecco's modified Eagle medium (Alpha-MEM; Invitrogen Life Technologies). The medium contained 10% fetal bovine serum (FBS GIBCO), 100 U/mL penicillin, and 100 μg/mL streptomycin. The bioceramic particles were kept in the culture medium for 1 and 5 days at 37°C. Afterward, the suspension was centrifugated at 4000 rpm for 20 min and passed through a 0.2 μm filter. The filtrate solution was stored for the cell culture assays.

Approximately 7500 cells were cultured with 500 μL of the bioceramic-conditioned medium (for 1 and 5 days) and incubated at 37°C in a humidified air atmosphere containing 5% CO_2. The cell viability was evaluated using the 3-(4,5-dimethylthiazol-2-yl)5-(3-carboxymethoxyphenyl)-2-(4-sulfophenyl)-2Htetrazolium (MTS) assay according to the protocol provided by the manufacturer (CellTiter Aqueous One Solution cell proliferation assay kit from Promega). MTS assays were performed in quadruplicate after 3, 5, and 7 days of cell culture. Briefly, after 2 h of incubation with the MTS reagent in a humidified 5% CO_2 atmosphere, the medium was collected from the samples and

absorbance was measured at a wavelength of 490 nm using an ELISA microplate reader (Tecan Infinite F-50).

The osteogenic differentiation of DPSCs in the presence of the nanobioceramic-conditioned medium was also evaluated. DPSCs, 6.5×10^3 cells, were seeded with the conditioned medium and maintained in basal culture medium for 7 days (DMEM supplemented with 10% FBS, 100 IU/mL penicillin, and 100 mg/mL streptomycin). The medium was changed every 3 days. After completing the incubation period, alkaline phosphatase (ALP) production was analyzed by nitroblue tetrazolium (NBT) 5-bromo-4-cloro-3-indolyl phosphate p-toluidine (BCIP) assay. ALP secreted by the osteogenically differentiated cells produces the cleavage of the phosphate group of BCIP, which generates a proton that reduces NBT to an insoluble purple precipitate. The intensity of enzyme activity associated with the cells was qualitatively examined by optical microscopy.

To analyze Runx2 gene expression, 2×10^5 cells were plated in 35 mm in duplicate. They underwent treatment for 48 hours with conditioned medium of 1 and 5 days. Total RNA was isolated with Trizol (GIBCO, Carlsbad, CA, USA) from control cells and those treated with conditioned medium. Complementary DNA was generated by M-MLV reverse transcriptase (Promega, Madison, WI, USA) using oligo (dT) (Promega) as primer and 1.0 μg of total RNA. Real-Time quantitative PCR reactions were performed using the following human-specific primers: RUNX-2, forward 5'-CAAGTA-GCAAGGTTCAACGA-3' and reverse 5'-CGGTCAGAG-AACAAACTAGG-3', PCR product size 205 bp, GADPH, forward 5'-CAAAATCAAGTGGGGCGATGCTG-3' and reverse 5'-TGTGGTCATGAGTCCTTCCACGAT-3', PCR product size 283 bp. The expression of GADPH was analyzed as a loading control. Quantitative PCR was performed with the real-time PCR system, LightCycler (Roche, Diagnostics, BS, SE). Each reaction was conducted in strips with 50 ng of cDNA, in a final volume of 10 μL. The PCR mixture contained LC FastStart DNA Master SYBR Green I (Roche Diagnostics, Basel, Switzerland), 3 mM $MgCl_2$, and 0.3 pmol of each primer (forward and reverse). Fluorescence was analyzed using LightCycler Analysis Software (Roche Diagnostics, BS, SE). The quantification of gene expression was determined through fold-change relative to the control condition.

3. Results and Discussion

3.1. Synthesis of Nanobioceramics. Figure 1 shows the characterization results of the synthesized nanobioceramics. XRD pattern of nHA is in agreement with the HA crystalline phase (JCPD 09-0432), whereas the nBG pattern confirms the amorphous nature of the BG structure. The low-angle XRD patterns of MBG and nMBG present the characteristic Bragg reflections corresponding to a highly ordered mesoporous structure. These low-angle XRD reflections are the result of an ordered hexagonal array of cylindrical nanopores, which is indexed assuming a hexagonal unit cell (space group p6mm) [21]. TEM images show that nHA and nBG present an estimated particle size of around 40 and 70 nm, respectively. MBG has a micrometric particle size of approximately 2.5 μm, whereas nMBG particles exhibit a spherical morphology of

TABLE 1: Elemental composition of nanobioceramics (wt.%) measured by EDX analysis.

| Bioceramic	O	Ca	P	Si	Na
nHA	14.34	57.39	28.27	—	—
nBG	16.47	43.34	14.67	25.53	—
MBG	22.80	13.86	0.88	62.46	—
nMBG	12.75	36.72	0.28	49.83	0.42

around 100 nm. HRTEM images of MBG and nMBG show that these materials present a honeycomb-like structure, consisting of a hexagonal close-pack array of nanopores. The diameter of the nanopores estimated from HRTEM images is around 4 nm. BET specific surface areas of nHA and nBG were 67 and 77 m^2/g, respectively. These nanoparticles are essentially nonporous, so the surface area values should be given mainly by the external surface area of the nanoparticles. MBG and nMBG presented surface area values as high as 488 and 443 m^2/g, which is consequence of the large internal surface provided by the highly ordered nanoporous structure. Table 1 presents the semiquantitative results of the chemical composition of the particles obtained by the EDX analysis. Calcium and phosphorous contents of nHA and siliceous nature of BG materials are confirmed. It can be noted that BG particles with nanoporous structure (MBG and nMBG) present a considerably lower content of phosphorus than that measured in the nBG particle, indicating that final phosphorous contents in nanoporous BG materials may differ more significantly from the nominal compositions.

Surface hydroxyl groups of the bioceramics were analyzed by FTIR-ATR in the 3000–4000 cm^{-1} range (Figure 2). IR spectra of the materials exhibit bands around 3657 and 3744 cm^{-1} corresponding to structural hydroxyl groups. In the case of nHA, the band at 3657 cm^{-1} is due to OH hydrogen bonded with phosphate group whereas the band around 3744 cm^{-1} has been assigned to O-H stretch where very little or no hydrogen bonding occurs [22]. In the FTIR-ATR spectra of BG materials, the 3744 cm^{-1} band may be attributed to O-H stretch of free silanol groups, whereas 3657 cm^{-1} vibration could be related to geminal silanols, which consist of two hydroxyl groups, that are attached to one silicon atom of the BG structure [23]. Among the BG materials studied, nMBG spectrum exhibits only the O-H stretch band with relatively low intensity, indicating that the microsized MBG presents a lower concentration of silanol groups on its surface.

Figure 3 schematizes the main structural characteristics of the nanomaterials and the synthesis route used for their preparation. Models of the molecular structure of HA and BG are also shown. nHA and nBG are essentially no porous materials with nanometric particle size. MBG and nMBG have a highly ordered hexagonal nanoporous structure with micrometric and nanometric particle size, respectively. HA is a hydroxylated calcium phosphate with a crystalline structure, which contrast with the amorphous and siliceous structure of BG.
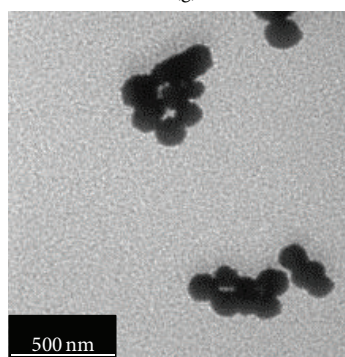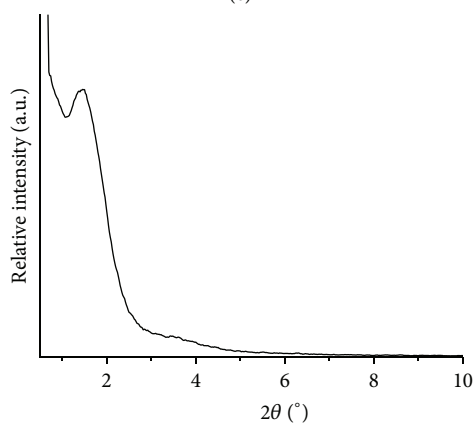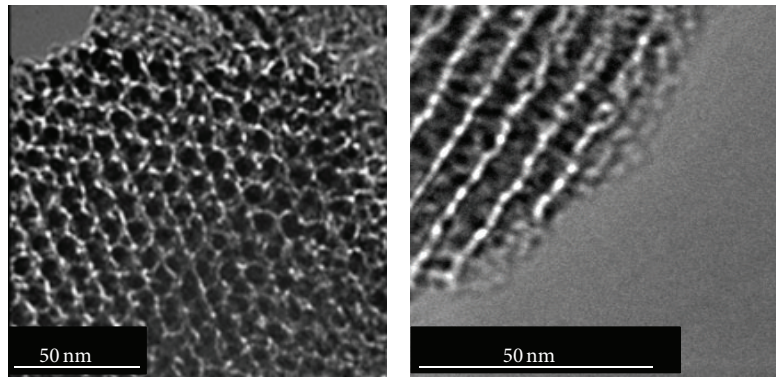
(a)

(e)

(b)

(f)

(c)

(g)

(d)
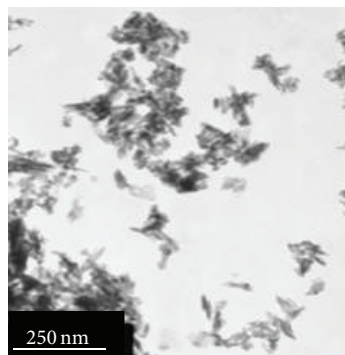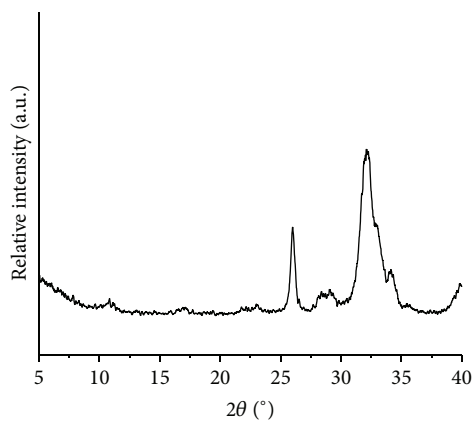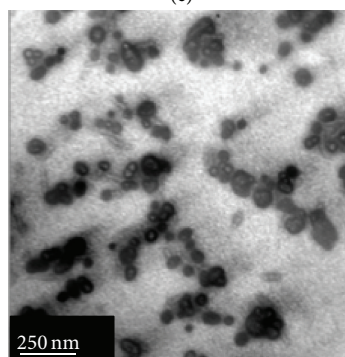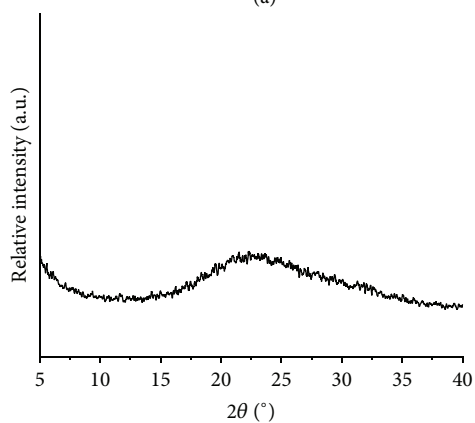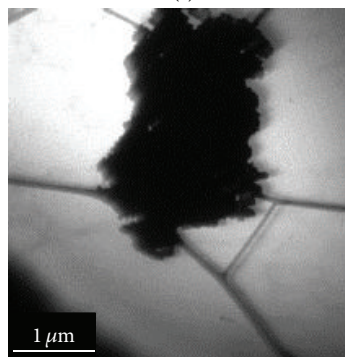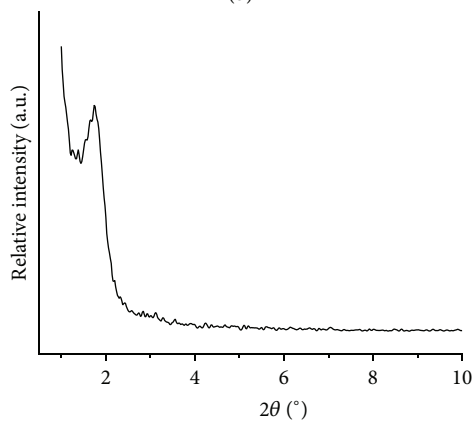
(h)

Figure 1: Continued.

	nHA	nBG	MBG	nMBG
Particle size (nm)	40	70	2500	100
Surface area (m^2/g)	67	77	488	443

(k)

FIGURE 1: Low-angle XRD patterns and TEM images of nHA (a, e), nBG (b, f), MBG (c, g), and nMBG (d, h). HRTEM images of MBG (i) and nMBG (j). Particle size and BET specific surface area of nanobioceramics (k).
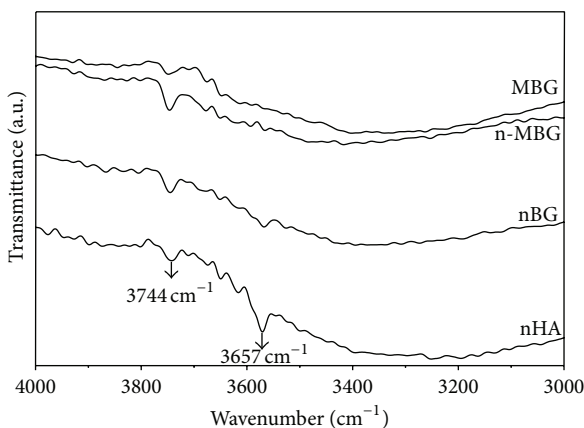

FIGURE 2: ATR-FTIR analysis of hydroxyl functional groups of the nanobioceramics after heat treatment at 150°C for 2 hours.

3.2. In Vitro Bioactivity Assays.

The ability of the bioceramics to induce the formation of bone-like apatite on its surface was assessed in SBF. Apatite crystallization can be analyzed by XRD (Figure 4) considering the intensity of the peak at 31.7° 2θ, corresponding to the 211 reflection of the apatite crystal (JCPD250166). XRD pattern of nHA does not undergo changes after the different immersion periods in SBF; particularly the intensity and shape of the reflection around 31.7° are maintained. In the case of BG nanomaterials, the apatite crystallization peak is observed in all XRD patterns (Figures 4(b)–4(d)). After 24 h of immersion in SBF, a faster apatite formation is observed on nBG than that produced on MBG and nMBG, as judged by the intensity of the 31.7° peak. Moreover, XRD pattern of MBG nanospheres after 72 h exhibits an apatite peak more intensive than that observed in the diffractogram of the microsized MBG. The evolution

of apatite formation on the bioceramic surfaces was also verified by FTIR-ATR analysis (Figure 5), mainly from the presence of two bands around 600 cm^{-1}, attributed to the P-O bending vibration and from another strong band in the 1000–1100 cm^{-1} area, attributed to the P-O symmetric stretching vibration in crystalline apatite [24]. The FTIR spectra of nHA soaked in SBF retain the characteristic bands of the unreacted nanoparticle. In the case of nBG, the doublet of bands centered at 560 and 600 cm^{-1} can be observed after 12 h, confirming a faster formation of crystalline apatite after short times of immersion in SBF. As the apatite layer begins to develop on the nanoparticle surface, the P-O stretching peak becomes more intense and sharper. The crystalline P-O vibrational bands in the MBG and nMBG spectra appear only after 72 h and present significantly lower intensity than that observed in the nBG spectra. Apatite mineralization on the nanobioceramic surfaces was also examined by SEM-EDX analysis (Figure 6). After immersion in SBF, nHA shows smooth and homogeneous surface, confirming the low apatite-forming ability of this nanobioceramic. In contrast, a higher degree of mineralization in terms of density, extension, and cluster mineral size can be seen on the nBG surface at early incubation period, which is increased with the immersion time in SBF. A similar precipitate morphology was observed on the MBG surface; however, these mineral deposits have a less crystalline structure as was already confirmed by XRD and FTIR analyses. nMBG exhibits a relatively smooth surface until 24 h of immersion in SBF. After 72 h, the presence of a dense mineralized layer covering all the nMBG is detected, with similar appearance to the mineral phase formed on nBG and MBG. Figure 6(b) shows the Ca and P contents of the mineralized surfaces determined by EDX analysis. It can be observed that BG nanomaterials present a marked increase in the total Ca and P contents with
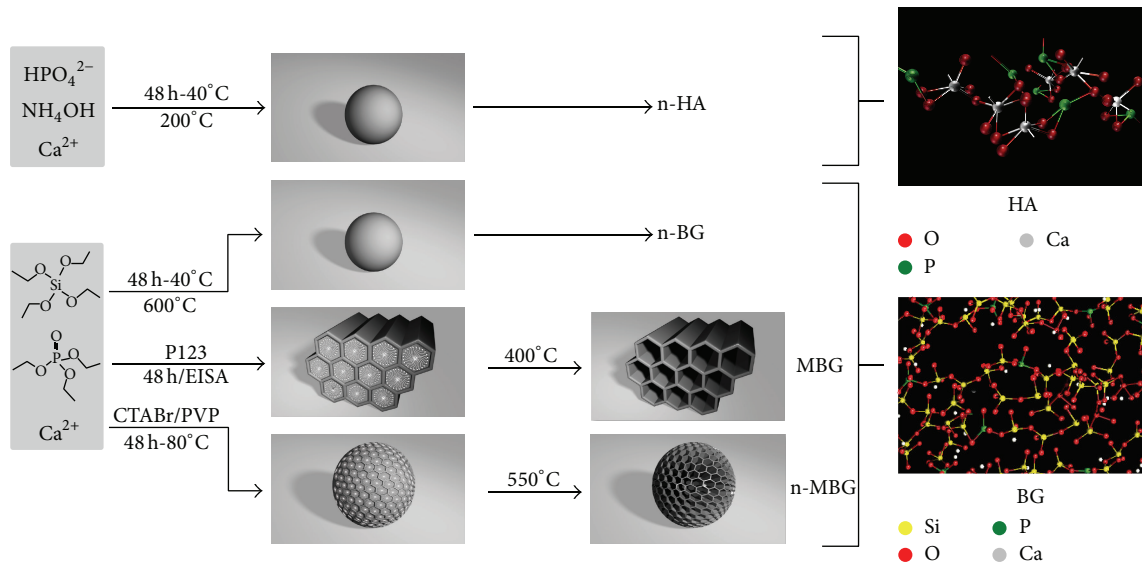
FIGURE 3: Schematic representation of the synthesis routes and main structural characteristics of nanobioceramics.

increasing time in SBF, whereas it increases slightly on the nHA surface, correlating well with the evolution of apatite formation observed in the previous analyses.

In order to explain the bioactive behavior of the nanobioceramics, the amounts of calcium phosphate and silicon released from the nanomaterials into Tris buffer at pH 7.4 were measured. Figure 7 shows the concentration of ions released per mass of bioceramic as a function of time. nBG and nMBG presented a marked release of Ca^{2+} within the first 3 days of immersion in Tris buffer. However, extremely low Ca^{2+} concentrations were released from nHA and MBG during the entire monitoring period. On the other hand, nBG also exhibited the highest PO_4^{3-} release concentrations after 2 days, reaching a maximum concentration at 1 day of immersion into solution. PO_4^{3-} release tend was similar for nHA, MBG, and nMBG, which could be related to the higher stability of the HA crystalline structure and the lower phosphorous contents of the MBG materials. No significant differences were detected in the concentration of silicon species (dissolved simple silicates, monomeric silica, and silicic acid) produced for the BG materials, which increased around 4 mM/g over the first 24 h of immersion.

The crystallization of the apatite phase on the bioceramics strongly depends on the concentration of ionic dissolution products in the surrounding fluid [25, 26]. As has already been mentioned, siliceous and more amorphous BG structure is more soluble and reactive than crystalline HA, thereby accelerating the apatite formation process through the ionic dissolution products. BG materials with nanometric particle size (nBG, nMBG) promoted a faster formation of apatite phase with a more crystalline structure. These results suggest that external surface area of the BG nanomaterials seems to affect the crystallization of apatite more significantly than the internal surface area of the nanoporous materials. Sepulveda et al. [27] found that the microsized glasses have a dissolution behavior that is directly correlated with their

particle size range, with the dissolution rate increasing as the particle size decreased. Mačković et al. [28] prepared bioactive glass (type 45S5) nanoparticles with a mean particle size in the range of 20–60 nm by flame spray synthesis. The BG nanoparticle confirmed higher surface reactivity compared with the micron-sized BG promoting a faster apatite formation after 1 day. In our study, nBG with particle size of ~70 nm and essentially no porous structure clearly presents the highest bioactive response, accelerating the crystallization of apatite after 24 hours of immersion in SBF. Although nMBG present a high surface area nanoporous structure and a particle size (~100 nm) slightly larger than nBG, apatite formation on this particle occurs only after 72 hours. This result could be due to the effect of nanoparticle size reduction from 100 to 70 nm on the crystallization process of apatite on the nanoparticle surface but also to the significantly lower phosphorous content released by the nMBG particle. In the case of MBG nanomaterials, it has been observed that nanopore sizes and surface areas directly relate to their bioactivity [29]. Large and accessible porosity, high surface area, and high material reactivity accelerate the Ca^{2+}-H^+ ionic exchange in SBF, establishing an acidic MBG surface that allows the formation of octacalcium phosphate (OCP) during the first hour, which is transformed into a deficient carbonatehydroxyapatite (CDHA) with increasing incubation time [16]. Ion transport from and toward the internal surface of MBG is limited by diffusion through the nanoporous channels, which should reduce the rate of crystallization of the apatite layer in relation to that formed through a no impeded ion diffusion process on the external surface of nBG. This ion exchange stage of the mechanism of apatite formation, low content of phosphorous, and surface silanol groups of the MBG particles can explain the lower apatite mineralization observed on MBG. Although MBG and nMBG presented significantly lower phosphorous content than the nBG, particle size reduction to nanometric
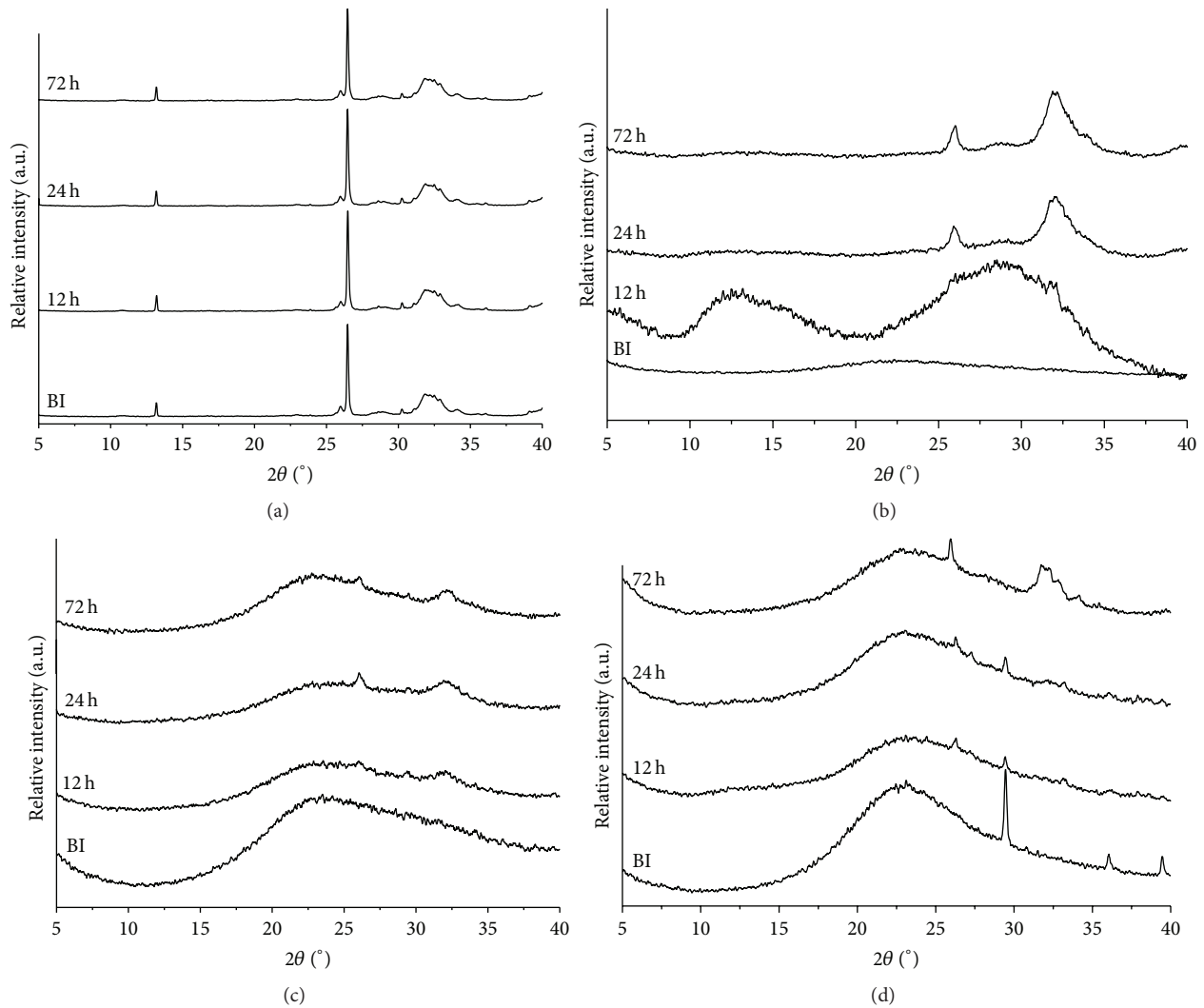
(a)

(b)

(c)

(d)

FIGURE 4: XRD analysis of nanobioceramics before (BI) and after different immersion times in SBF: (a) nHA, (b) nBG, (c) MBG, and (d) nMBG.

dimensions seems to accelerate the formation of apatite on the BG materials, rather than an internal surface area provided by the nanoporous structure.

3.3. Protein Adsorption. The protein adsorption capacity of the bioceramics is also an important property that affects their bioactivity by influencing the cellular attachment, proliferation, migration, and differentiation [30]. BSA was used as model of extracellular protein to study the protein affinity of the nanobioceramic surfaces. From Figure 8(a), it can be observed that the protein adsorption capacity of nHA was higher than that presented by the BG nanoceramics, and a larger amount of protein is adsorbed on the BG materials with nanometric particle size (nBG and nMBG). FTIR-ATR spectra of protein adsorbed on the nanobioceramic surfaces exhibit the characteristic bands of amide group at 1600–1690 cm^{-1} (amide I, C=O stretching), 1480–1575 cm^{-1} (amide II, CN stretching, NH bending), and 1229–1301 cm^{-1} (amide III CN stretching, NH bending) [31]. The intensity of

these bands is higher in the FTIR spectrum of the proteins adsorbed on nHA than that observed in the spectra of the BG materials. Particularly, amide vibrations of proteins adsorbed on MBG are weakly detected. Protein adsorption process on the bioceramics depends on several factors, such as chemical composition, surface charge, particle size, specific surface area, and porosity of the materials [32]. Ca^{+2} and PO_4^{3-} constitute the main binding sites for protein adsorption on bioceramic surfaces [33], which could explain the higher amount of protein adsorbed on nHA compared with that adsorbed on the siliceous BG materials. In addition, BG has a higher solubility than HA, which has been found to increase the medium pH, producing a negative charge on the glass surface that may reduce the affinity with the negatively charged proteins [34]. On the other hand, protein adsorption was relatively lower on microsized MBG particle. Although MBG has a high specific surface area, the adsorption of BSA with 4 nm × 4 nm × 14 nm dimensions on the internal MBG surface is probably limited through nanopore openings of
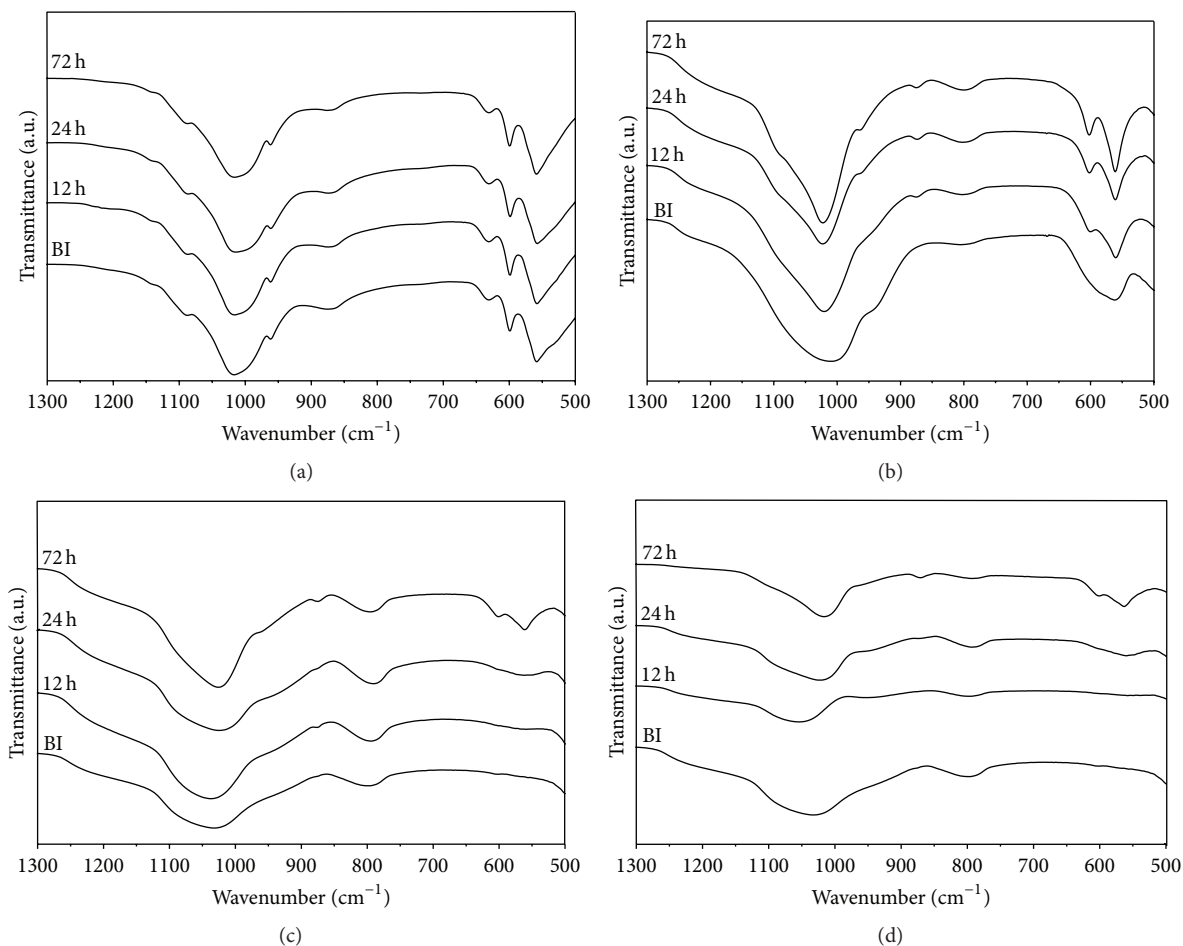
(a)

(b)

(c)

(d)

FIGURE 5: ATR-FTIR analysis of nanobioceramics before (BI) and after different immersion times in SBF: (a) nHA, (b) nBG, (c) MBG, and (d) nMBG.

4 nm. This effect was also observed for protein adsorption on nanocrystalline Zn-containing hydroxyapatite with different porosity [35] where it was concluded that the pore size is the major factor controlling the selective adsorption of serum proteins. In the current study, adsorption of BSA on the bioceramics should take place mainly on the external surface of the particle, which is favored on bioceramics with smaller nanometric particle size having higher external surface area.

3.4. Cell Culture. The effect of bioceramic-conditioned media (for 1 and 5 days) on the proliferation and differentiation of DPSCs was also assessed. Figure 9 shows that MTS absorbance of cells cultured in the different conditioned media tended to be slightly higher than that of control culture, confirming that the nanomaterial extracts do not affect viability of DPSCs. The increase of cell viability produced by the BG conditioned media has been also observed by other authors [36]. This effect is attributed to the alkalinization produced by ion exchange between BG and medium, which increases the sensitivity of calcium channels of the cell membrane, enhancing cellular calcium entry.

The osteogenic differentiation of DPSCs was assessed by detecting the production of ALP enzyme and the gene expression of Runx2. ALP can easily be detected using BCIP/NBT as a substrate, which stains cells blue-violet when ALP is present. From Figure 10, it can be observed that when DPSCs are cultured with 1-day nanobioceramic-conditioned media, significant ALP staining is only observed in the cells cultured with the nBG extract. On the other hand, cells cultured in media treated with BG materials for 5 days produce equivalent ALP staining, except the cells incubated in nHA medium, which exhibit a relatively low production of ALP. The expression of osteogenic gene Runx2 was also detected in all the nanobioceramic-conditioned cell cultures (Figure 11). The expression of Runx2 was particularly upregulated for the DPSCs cultured with the nBG and nMBG extracts. ALP and Runx2 are considered early markers of osteogenic differentiation process of stem cells, which are expressed when bone-forming osteoblasts lay down the bone extracellular matrix [37, 38]. The capability of microsized BG to promote the upregulation of ALP and Runx2 has seen demonstrated in several studies [39, 40]. Osteogenic differentiation properties of BG have been largely attributed to the effect of specific concentrations of its ionic dissolution products (silicon) [41], which also favors the osteoblast metabolic activity through an increase in the extracellular pH [42]. In the current
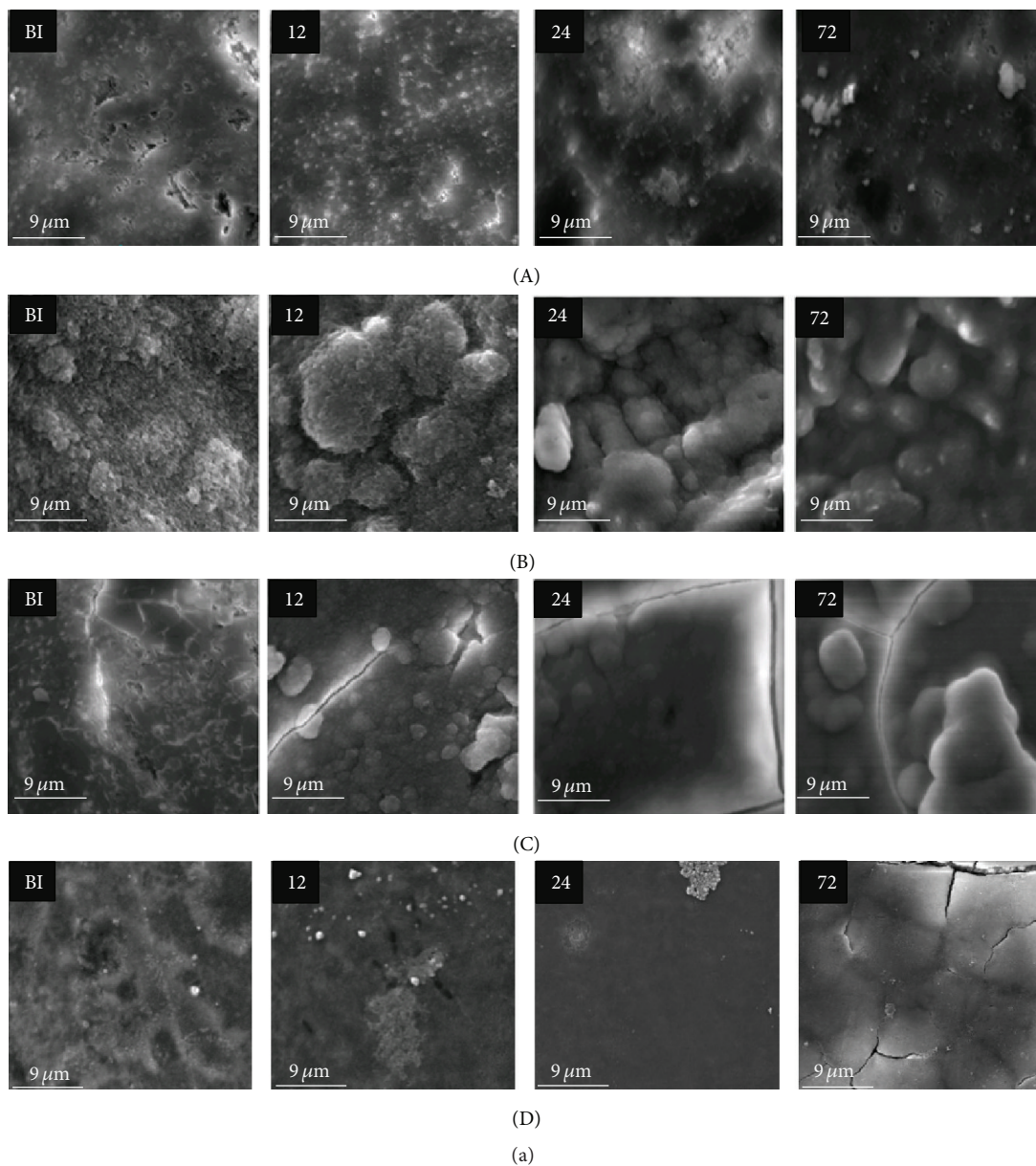
(a)

(b)

FIGURE 6: SEM images (a) and EDX Ca + P content (b) of nanobioceramic surfaces after different immersion times in SBF: (A) nHA, (B) nBG, (C) MBG, and (D) nMBG.
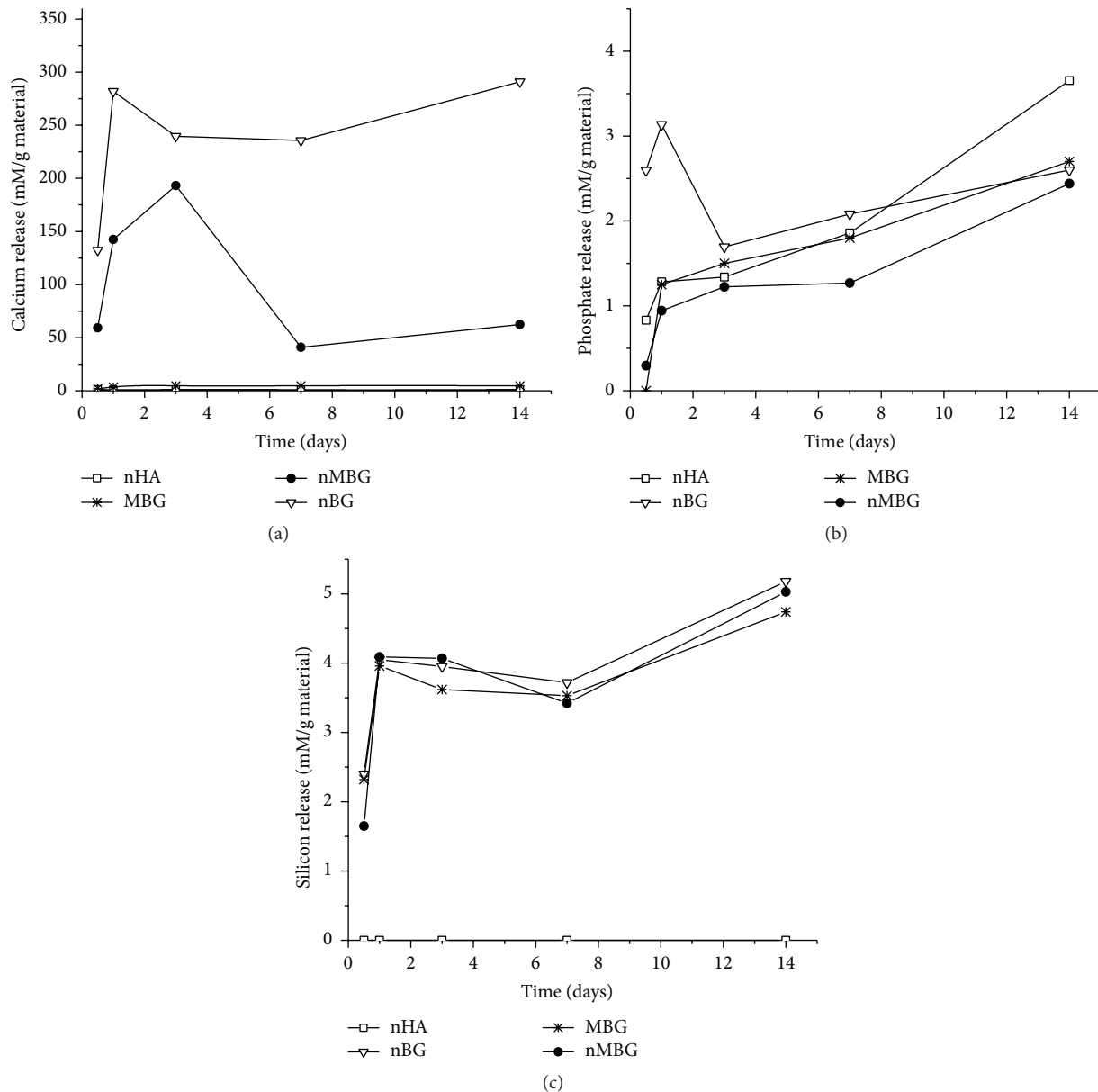
(a)

(b)

(c)

FIGURE 7: Cumulative ion release from nanobioceramics incubated in Tris buffer solution pH 7.4. The concentration of ion released into the solution was expressed as ion concentration per bioceramic mass (mM/g).

study, the silicon concentrations released into buffer Tris pH 7.4 measured by an ASTM photometric method did not reveal significant differences among the studied bioceramics. However, Ca^{2+} concentrations were found to be higher in the dissolution products of nBG and nMBG, and higher PO_4^{3-} concentrations were also detected in the nBG extracts. Specific Ca^{2+} concentrations have been found to be suitable for osteoblast proliferation, differentiation, and extracellular matrix (ECM) mineralization [43]. Ca^{2+} also increases the expression of insulin growth factors that regulate osteoblast proliferation as well as the release of glutamate, which is known is involved in bone mechanosensitivity mechanism [44]. On the other hand, it has been also demonstrated that

PO_4^{3-} regulates the expression of the matrix Gla protein (MGP) in osteoblasts [45], a key regulator of bone formation.

As has already been discussed, high surface area of bioceramics with nanometric dimensions increases their solubility, and consequently the release of ionic products with osteostimulative capacity. This effect is particularly marked for nBG, which presents the smallest nanoparticle size and therefore higher external surface available for ion dissolution without pore diffusion limitations. Rapid dissolution of nBG enables the formation of a bioactive extracellular medium after 1 day of incubation, which is capable of upregulating key osteogenic markers involved in the development of a mineralized phenotype. It is worth emphasizing that all
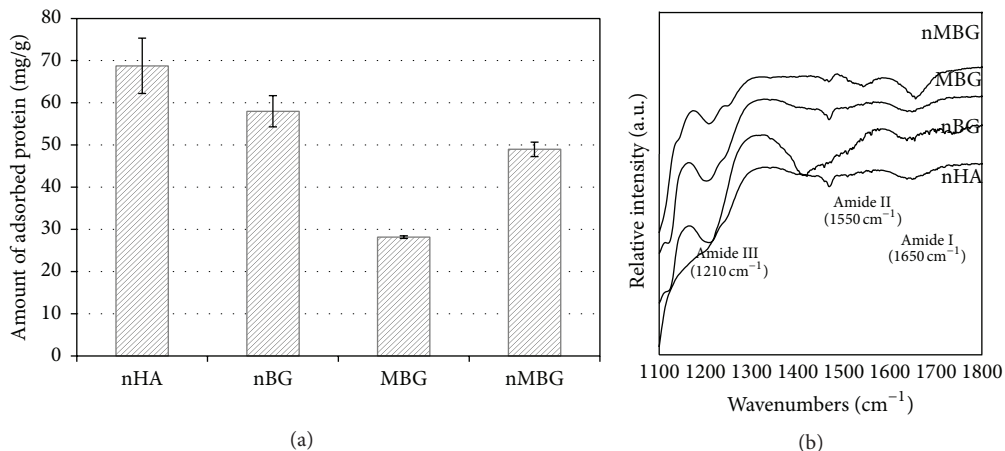
(a)

(b)

FIGURE 8: Amount of adsorbed protein on the nanobioceramic surfaces after 6 h of incubation in a 0.4 mg/mL BSA solution (a). ATR-FTIR analysis of proteins adsorbed on the nanobioceramic surfaces (b).
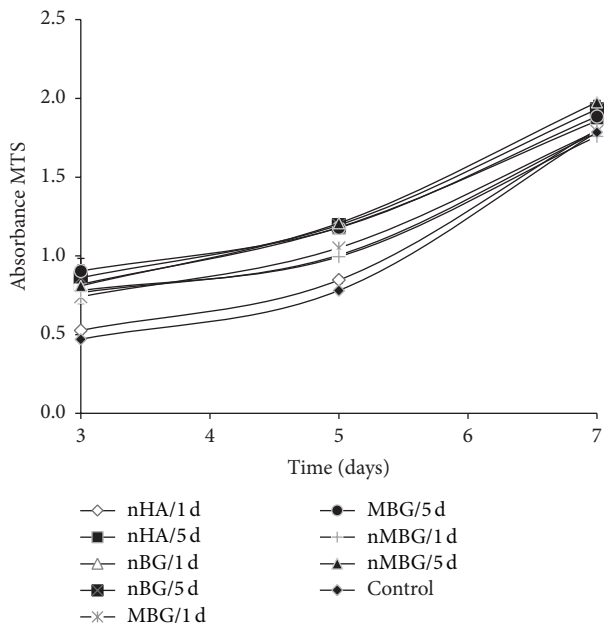

FIGURE 9: Viability (MTS) of DPSCs cultured in 1- and 5-day nanobioceramic-conditioned media at different culture times.
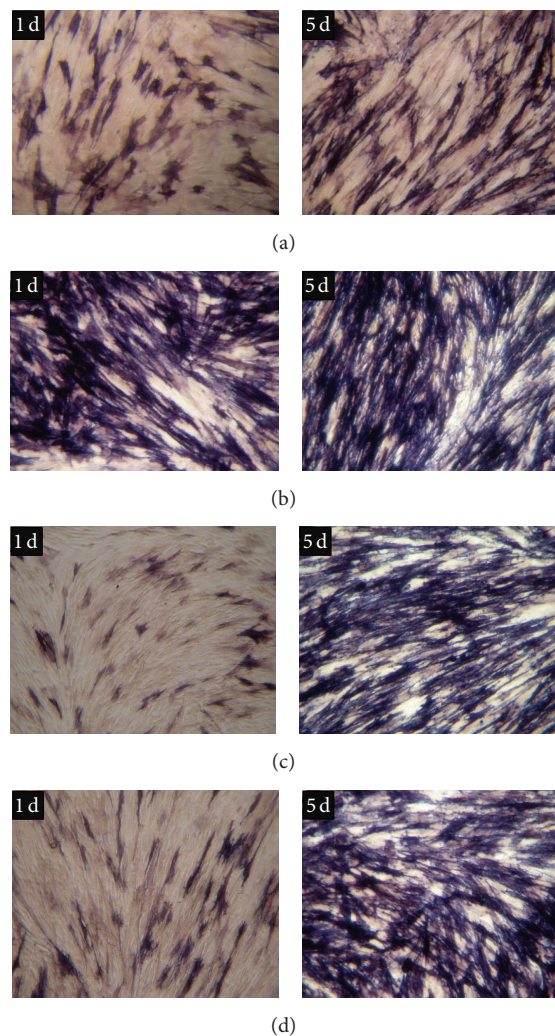

FIGURE 10: Alkaline phosphatase production detected with BCIP/NBT staining in DPSCs cultured in 1- and 5-day nHA (a), nBG (b), MBG (c), and nMBG (d) conditioned media.

nanobioceramics were able to stimulate the osteogenic differentiation of DPSCs in absence of osteogenic factors, which is an important aspect for bone tissue engineering applications. In addition, the capability of nBG for accelerating the *in vitro* apatite crystallization, as well as the osteogenic differentiation of stem cells, suggests that this bioactive nanoparticle could be useful for promoting rapid bone tissue repair.

4. Conclusion

This study demonstrates the effect of nanoscale structural properties of nanobioceramic particles on their *in vitro*
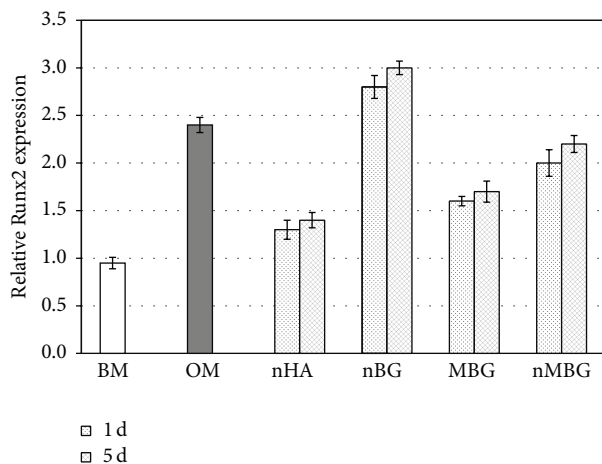
Figure 11: Relative Runx2 expression in DPSCs cultured for 48 hours with 1- and 5-day nanobioceramic-conditioned media.

bioactivity and stem cell response. HA and BG nanoceramics were found to present different bioactive response depending on their chemical composition, nanoparticle size, surface area, and porosity. In general, BG nanomaterials present higher bioactivity in SBF than HA due to the less crystalline and more reactive nature of the glass structure. The nano-metric particle size of BG seems to be more determining in controlling the concentration of ionic dissolution products and therefore the bioactivity compared to their nanoporous structure. It is postulated that higher external surface area of nBG nanoparticles enables rapider glass dissolution as compared with the internal and less accessible surface area provided by the MBG nanoporous structure. Short disso-lution periods of nBG also produce bioactive extracellu-lar media capable of upregulating key osteogenic markers involved in the development of a mineralizing phenotype in DPSCs. The bioactive properties exhibited by nBG appear promising for accelerating the bone regeneration process in tissue engineering applications.

Conflict of Interests

The authors declare that there is no conflict of interests regarding the publication of this paper.

Acknowledgments

References

[1] L. L. Hench, "Bioceramics: from concept to clinic," *Journal of the American Ceramic Society*, vol. 74, no. 7, pp. 1487–1510, 1991.

[2] S. M. Best, A. E. Porter, E. S. Thian, and J. Huang, "Bioceramics: past, present and for the future," *Journal of the European Ceramic Society*, vol. 28, no. 7, pp. 1319–1327, 2008.

[3] L. L. Hench, I. D. Xynos, and J. M. Polak, "Bioactive glasses for in situ tissue regeneration," *Journal of Biomaterials Science, Polymer Edition*, vol. 15, no. 4, pp. 543–562, 2004.

[4] S. G. Caridade, E. G. Merino, N. M. Alves, V. D. Z. Bermudez, A. R. Boccaccini, and J. F. Mano, "Chitosan membranes con-taining micro or nano-size bioactive glass particles: evolution of biomineralization followed by in situ dynamic mechanical analysis," *Journal of the Mechanical Behavior of Biomedical Materials*, vol. 20, no. 1, pp. 173–183, 2013.

[5] A. Lukowiak, J. Lao, J. Lacroix, and J.-M. Nedelec, "Bioactive glass nanoparticles obtained through sol-gel chemistry," *Chem-ical Communications*, vol. 49, no. 59, pp. 6620–6622, 2013.

[6] K. P. Sanosh, M.-C. Chu, A. Balakrishnan, Y.-J. Lee, T. N. Kim, and S.-J. Cho, "Synthesis of nano hydroxyapatite powder that simulate teeth particle morphology and composition," *Current Applied Physics*, vol. 9, no. 6, pp. 1459–1462, 2009.

[7] M. P. Ferraz, F. J. Monteiro, and C. M. Manuel, "Hydroxyapatite nanoparticles: a review of preparation methodologies," *Journal of Applied Biomaterials & Biomechanics*, vol. 2, no. 2, pp. 74–80, 2004.

[8] T. J. Webster, C. Ergun, R. H. Doremus, R. W. Siegel, and R. Bizios, "Enhanced functions of osteoblasts on nanophase ceramics," *Biomaterials*, vol. 21, no. 17, pp. 1803–1810, 2000.

[9] T. J. Webster, C. Ergun, R. H. Doremus, R. W. Siegel, and R. Bizios, "Specific proteins mediate enhanced osteoblast adhe-sion on nanophase ceramics," *Journal of Biomedical Materials Research*, vol. 51, no. 3, pp. 475–483, 2000.

[10] M. Vollenweider, T. J. Brunner, S. Knecht et al., "Remineraliza-tion of human dentin using ultrafine bioactive glass particles," *Acta Biomaterialia*, vol. 3, no. 6, pp. 936–943, 2007.

[11] F. Valenzuela, C. Covarrubias, C. Martínez, P. Smith, M. Díaz-Dosque, and M. Yazdani-Pedram, "Preparation and bioactive properties of novel bone-repair bionanocomposites based on hydroxyapatite and bioactive glass nanoparticles," *Journal of Biomedical Materials Research Part B Applied Biomaterials*, vol. 100, no. 6, pp. 1672–1682, 2012.

[12] S. K. Misra, D. Mohn, T. J. Brunner et al., "Comparison of nanoscale and microscale bioactive glass on the properties of P(3HB)/Bioglass composites," *Biomaterials*, vol. 29, no. 12, pp. 1750–1761, 2008.

[13] X. Yan, C. Yu, X. Zhou, J. Tang, and D. Zhao, "Highly ordered mesoporous bioactive glasses with superior in vitro bone-forming bioactivities," *Angewandte Chemie—International Edi-tion*, vol. 43, no. 44, pp. 5980–5984, 2004.

[14] C. Wu, W. Fan, and J. Chang, "Functional mesoporous bioactive glass nanospheres: synthesis, high loading efficiency, control-lable delivery of doxorubicin and inhibitory effect on bone cancer cells," *Journal of Materials Chemistry B*, vol. 1, no. 21, pp. 2710–2718, 2013.

[15] Z. Hong, R. L. Reis, and J. F. Mano, "Preparation and in vitro characterization of novel bioactive glass ceramic nanoparticles," *Journal of Biomedical Materials Research—Part A*, vol. 88, no. 2, pp. 304–313, 2009.

[16] A. López-Noriega, D. Arcos, I. Izquierdo-Barba, Y. Sakamoto, O. Terasaki, and M. Vallet-Regí, "Ordered mesoporous bioac-tive glasses for bone tissue regeneration," *Chemistry of Materi-als*, vol. 18, no. 13, pp. 3137–3144, 2006.

[17] T. Kokubo, H. Kushitani, S. Sakka, T. Kitsugi, and T. Yamamuro, "Solutions able to reproduce in vivo surface-structure changes

in bioactive glass-ceramic A-W[3]," *Journal of Biomedical Materials Research*, vol. 24, no. 6, pp. 721–734, 1990.

[18] ASTM International, "Standard test method for silica in water," Designation D859-00, ASTM International, West Conshohocken, Pa, USA, 2000.

[19] Z. Marczenko, *Separation and Spectrophotometric Determination of Elements*, Ellis Horwood, Chichester, UK, 1986.

[20] C. Balanda, *Stem cells isolation from dental tissues and their osteogenic differentiation capacity [Dissertation]*, University of Chile, 2014.

[21] Y. Lu, R. Ganguli, C. A. Drewien et al., "Continuous formation of supported cubic and hexagonal mesoporous films by sol-gel dip-coating," *Nature*, vol. 389, no. 6649, pp. 364–368, 1997.

[22] R. N. Pandaa, M. F. Hsieha, R. J. Chunga, and T. S. Chin, "FTIR, XRD, SEM and solid state NMR investigations of carbonate-containing hydroxyapatite nano-particles synthesized by hydroxide-gel technique," *Journal of Physics and Chemistry of Solids*, vol. 64, no. 2, pp. 193–199, 2003.

[23] E. F. Vansant, P. Van Der Voort, and K. C. Vrancken, "The surface chemistry of silica," in *Characterization and Chemical Modification of the Silica Surface*, pp. 59–60, Elsevier Science, Amsterdam, The Netherlands, 1995.

[24] L. L. Hench, "Characterization of bioceramics," in *An Introduction to Bioceramics*, L. L. Hench, Ed., pp. 530–531, Imperial College Press, London, UK, 2nd edition, 2013.

[25] G. Daculsi, R. Z. LeGeros, and D. Mitre, "Crystal dissolution of biological and ceramic apatites," *Calcified Tissue International*, vol. 45, no. 2, pp. 95–103, 1989.

[26] R. Z. Legeros, I. Orly, M. Gregoire, and J. Kaimiroff, "Comparative properties and in vitro transformation of HA ceramics in serum," *Journal of Dental Research*, vol. 67, Abstract #152, p. 177, 1988.

[27] P. Sepulveda, J. R. Jones, and L. L. Hench, "In vitro dissolution of melt-derived 45S5 and sol-gel derived 58S bioactive glasses," *Journal of Biomedical Materials Research*, vol. 61, no. 2, pp. 301–311, 2002.

[28] M. Mačković, A. Hoppe, R. Detsch et al., "Bioactive glass (type 45S5) nanoparticles: in vitro reactivity on nanoscale and biocompatibility," *Journal of Nanoparticle Research*, vol. 14, pp. 966–987, 2012.

[29] W. Xia and J. Chang, "Well-ordered mesoporous bioactive glasses (MBG): a promising bioactive drug delivery system," *Journal of Controlled Release*, vol. 110, no. 3, pp. 522–530, 2006.

[30] C. J. Wilson, R. E. Clegg, D. I. Leavesley, and M. J. Pearcy, "Mediation of biomaterial-cell interactions by adsorbed proteins: a review," *Tissue Engineering*, vol. 11, no. 1-2, pp. 1–18, 2005.

[31] S.-S. Cheng, K. K. Chittur, C. N. Sukenik, L. A. Culp, and K. Lewandowska, "The conformation of fibronectin on self-assembled monolayers with different surface composition: an FTIR/ATR study," *Journal of Colloid and Interface Science*, vol. 162, no. 1, pp. 135–143, 1994.

[32] K. Wang, C. Zhou, Y. Hong, and X. Zhang, "A review of protein adsorption on bioceramics," *Interface Focus*, vol. 2, no. 3, pp. 259–277, 2012.

[33] B. Feng, J. Chen, and X. Zhang, "Interaction of calcium and phosphate in apatite coating on titanium with serum albumin," *Biomaterials*, vol. 23, no. 12, pp. 2499–2507, 2002.

[34] S. Lin, W. Van den Bergh, S. Baker, and J. R. Jones, "Protein interactions with nanoporous sol-gel derived bioactive glasses," *Acta Biomaterialia*, vol. 7, no. 10, pp. 3606–3615, 2011.

[35] E. Fujii, M. Ohkubo, K. Tsuru et al., "Selective protein adsorption property and characterization of nano-crystalline zinc-containing hydroxyapatite," *Acta Biomaterialia*, vol. 2, no. 1, pp. 69–74, 2006.

[36] P. Valerio, M. M. Pereira, A. M. Goes, and M. F. Leite, "The effect of ionic products from bioactive glass dissolution on osteoblast proliferation and collagen production," *Biomaterials*, vol. 25, no. 15, pp. 2941–2948, 2004.

[37] T. Komori, "A fundamental transcription factor for bone and cartilage," *Biochemical and Biophysical Research Communications*, vol. 276, no. 3, pp. 813–816, 2000.

[38] T. Komori, "Runx2, a multifunctional transcription factor in skeletal development," *Journal of Cellular Biochemistry*, vol. 87, no. 1, pp. 1–8, 2002.

[39] I. D. Xynos, M. V. J. Hukkanen, J. J. Batten, L. D. Buttery, L. L. Hench, and J. M. Polak, "Bioglass 45S5 stimulates osteoblast turnover and enhances bone formation in vitro: implications and applications for bone tissue engineering," *Calcified Tissue International*, vol. 67, no. 4, pp. 321–329, 2000.

[40] S. Hattar, A. Asselin, D. Greenspan, M. Oboeuf, A. Berdal, and J.-M. Sautier, "Potential of biomimetic surfaces to promote in vitro osteoblast-like cell differentiation," *Biomaterials*, vol. 26, no. 8, pp. 839–848, 2005.

[41] I. D. Xynos, A. J. Edgar, L. D. K. Buttery, L. L. Hench, and J. M. Polak, "Ionic products of bioactive glass dissolution increase proliferation of human osteoblasts and induce insulin-like growth factor II mRNA expression and protein synthesis," *Biochemical and Biophysical Research Communications*, vol. 276, no. 2, pp. 461–465, 2000.

[42] I. A. Silver, J. Deas, and M. Erecińska, "Interactions of bioactive glasses with osteoblasts in vitro: effects of 45S5 Bioglass, and 58S and 77S bioactive glasses on metabolism, intracellular ion concentrations and cell viability," *Biomaterials*, vol. 22, no. 2, pp. 175–185, 2001.

[43] S. Maeno, Y. Niki, H. Matsumoto et al., "The effect of calcium ion concentration on osteoblast viability, proliferation and differentiation in monolayer and 3D culture," *Biomaterials*, vol. 26, no. 23, pp. 4847–4855, 2005.

[44] P. J. Marie, "The calcium-sensing receptor in bone cells: a potential therapeutic target in osteoporosis," *Bone*, vol. 46, no. 3, pp. 571–576, 2010.

[45] M. Julien, S. Khoshniat, A. Lacreusette et al., "Phosphate-dependent regulation of MGP in osteoblasts: role of ERK1/2 and Fra-1," *Journal of Bone and Mineral Research*, vol. 24, no. 11, pp. 1856–1868, 2009.